One-step hydrothermal synthesis of a green NiCo-LDHs-rGO composite for the treatment of lead ion in aqueous solutions

Ata Makarem[1], Alireza Aldaghi[2,3], Mohammad Gheibi[4], Mohammad Eftekhari[5], Kourosh Behzadian[6,7*]

[1]*Department of Chemistry, University of Hamburg; Hamburg, Germany*

[2]*Department of Mechanical Engineering, Ferdowsi University of Mashhad, Mashhad, Iran*

[3]*Center for Nanotechnology in Renewable Energies, Ferdowsi University of Mashhad, Mashhad, Iran*

[4]*Institute for Nanomaterials, Advanced Technologies and Innovation, Technical University of Liberec, Studentská 1402/2, 461 17 Liberec 1, Czech Republic*

[5]*Department of Chemistry, Faculty of Sciences, University of Neyshabur, Neyshabur, Iran*

[6]*School of Computing and Engineering, University of West London; London, UK*

Email: kourosh.behzadian@uwl.ac.uk (Corresponding author)

[7]*Department of Civil, Environmental and Geomatic Engineering, University College London, UK*

Abstract

In this study, we have synthesised a microspherical nickel-cobalt-layered double hydroxides-reduced graphene oxide composite (NiCo-LDHs-rGO) through a one-step hydrothermal method. We subsequently used this composite as an adsorbent to remove Pb^{2+} from aqueous solutions. The instruments used for the characterisation of adsorbent included Fourier Transform Infrared Spectrophotometry (FT-IR), Field Emission Scanning Electron Microscopy (FESEM), Mapping Elemental Analysis, Electron Dispersive X-Ray spectroscopy (EDX), X-Ray Diffraction Analysis (XRD) and Brunauer-Emmett-Teller (BET)analysis. We conducted a series of experiments to investigate the factors affecting the adsorption of Pb^{2+} ions in batch mode such as solution pH, adsorbent dosage, contact time, competing ion and regeneration by NiCo-LDHs-rGO. Under optimised conditions determined using the Taguchi method (pH = 5.0, adsorbent dosage = 20 mg and contact time = 30 min), the best removal rate of 99.7% was achieved for 100 mg L^{-1} of Pb^{2+}. According to the results, NiCo-LDHs-rGO exhibited a high preference for Pb^{2+} over Cu^{2+}, Zn^{2+} and Cd^{2+}. This adsorbent was regenerated for several cycles (using 0.01 M HCl) with no significant deterioration in performance. The analyses of the adsorption isotherm models revealed that the adsorption of Pb^{2+} followed Freundlich isotherm with a maximum adsorption capacity of 200 mg g^{-1}. The kinetic data also confirmed that pseudo second order kinetic equation is the most accurate model for predicting the adsorption kinetics. Furthermore, the Simulink modelling illustrated that the adsorption kinetics of Pb^{2+} onto NiCo-LDHs-rGO could be accurately represented in a continuous stirred-tank reactor. Finally, dual interactions of the effective parameters can be modelled by polynomial equations in MATLAB, and according to the Taguchi model, pH emerged as the most influential factor among all the parameters.

Keywords: Nickel cobalt layered double hydroxides particles-reduced graphene oxide (NiCo-LDHs-rGO), Lead ion removal, Water treatment

1 Introduction

Lead (Pb) is a highly toxic element with notable impacts on renal function as well as the reproductive and nervous systems [1]. Due to its widespread industrial use of lead in batteries, alloys, pigments, plastic stabiliser, ammunition, glazes and etc., its release into the environment and surface runoff poses a significant environmental challenge [2, 3]. According to the reports of Centres for Disease Control and Prevention, the standard maximum levels of Pb^{2+} for adults and children are 100 μg/L and 50 μg/L, respectively [4]. Adsorption stands as the most commonly used technique for the removal of both organic and inorganic pollutants. A wide range of efficient natural and synthetic adsorbents could be used for this purpose [5-10]. Reusability of adsorbents and ease of operation are considered as other advantages of this method [11-15]. In this context, graphene oxide (GO) has been extensively used for the decontamination of water samples [16-18]. Due to the presence of hydroxyl, epoxy and carboxylic acid groups within its structure, GO is naturally hydrophilic and can also be modified with different functional groups for developing new adsorbents [19, 20]. In 2018, Eftekhari et al. modified GO with tannic acid for the elimination of Pb^{2+} in water samples, resulting in a nanocomposite with an adsorption capacity of 250 mg g^{-1} [21]. In 2021, Ghadirimoghaddam et al. used a GO-cyanuric acid nanocomposite for the preconcentration/removal of Pb^{2+}, achieving a calculated adsorption capacity of 333 mg g^{-1} [22]. Due to the convenient fabrication, environmental-friendly and high electrochemical activities, transition metal hydroxides have drawn much attention in the area of supercapacitors [23] and electrocatalysts [24, 25]. Despite their high surface area, layered double hydroxides (LDHs) have a high tendency to form aggregation – due to hydrogen-bonding interactions – which consequently reduces the available active sites [26]. To overcome this drawback, materials with high surface-area such as graphene [27] and carbon nanotubes [28] can be considered as modifiers.

The purpose of this study is to introduce a new cost-efficient and green adsorbent for Pb^{2+} treatment. Hence, we have synthesised a microspherical NiCo-LDHs-rGO composite using a one-step hydrothermal method. Subsequently, we evaluated it effectiveness in removing Pb^{2+} from aqueous media. Characterisation of the synthesised composite was carried out by FE-SEM, XRD, EDX, Mapping Elemental Analysis and FT-IR spectrophotometry. The parameters affecting the removal percentage of Pb^{2+} were optimised by the Taguchi design method, while the kinetics and mechanism of adsorption were investigated by different kinetic and isotherm models.

2 Experimental

2.1 Instruments

The following instruments and techniques were used in this study: (1) A BRNO-Mira3 LMU instrument manufactured by TESCAN in Czech Republic for FE-SEM, EDX and Mapping Elemental Analysis. FE-SEM was used to visualise the microstructure and surface morphology of the composite. EDX provided information concerning the elemental composition of the composite while Mapping Elemental Analysis enabled the spatial distribution of elements within the composite; (2) FT-IR spectra were recorded using an AVATAR 370 (USA); (3) The XRD analysis was carried out using a D8-Advance Bruker Cu Kα1 instrument (USA); (4) The specific surface area of the composite was determined using a Belsorp-Mini instrument (Japan) ; (5) In order to quantify the Pb^{2+} concentration (after adsorption), an electrothermal atomic absorption spectrometer equipped with a Pb hollow cathode lamp (283.3 nm) was used (Perkin Elmer Analyst 700, USA). Argon (99.99 %) was used as the inert atmosphere, with a flow rate of 300 mL min^{-1} during drying, ashing and cleaning stages and zero during the atomisation step; (6) For pH adjustment during the adsorption experiments, a Metrohm 827 pH-meter (Switzerland) was used; (7) The separation of the adsorbent from the solution was carried out using an Andreas Hettich D72 centrifuge instrument (Germany).

2.2 Reagents

Lead nitrate (Merck, Germany) was used to make a 1000 mg L^{-1} Pb^{2+} solution. Graphite (99.9%), $Co(NO_3)_2.6H_2O$ (99.5%), $Ni(NO_3)_2.6H_2O$ (99.5%), H_2SO_4 (98.0%), $KMnO_4$ (99.0%), H_2O_2 (30.0%), thiourea and HNO_3 (65.0%) were supplied by Merck (Germany).

2.3 Synthesis of GO and NiCo-LDHs-rGO

The steps for synthesising GO and NiCo-LDHs-rGO are as follows: (1) GO was first synthesised according to the Hummers method as presented in Fig. 1 [21]; (2) The NiCo-LDHs-rGO composite was then synthesised according to the following protocol: GO (0.35 g) underwent ultrasonication in 50 mL of deionised water for 45 minutes. $Co(NO_3)_2.6H_2O$ (0.40 g), $Ni(NO_3)_2.6H_2O$ (0.30 g) and thiourea (0.10) were then added to the solution; (3) The resulting mixture underwent an additional 30 minutes of ultrasonication and was subsequently autoclaved at 160 °C for 4 hours;

(4) The resulting composite was washed with deionised water three times and dried at 90 °C for 6 hours.

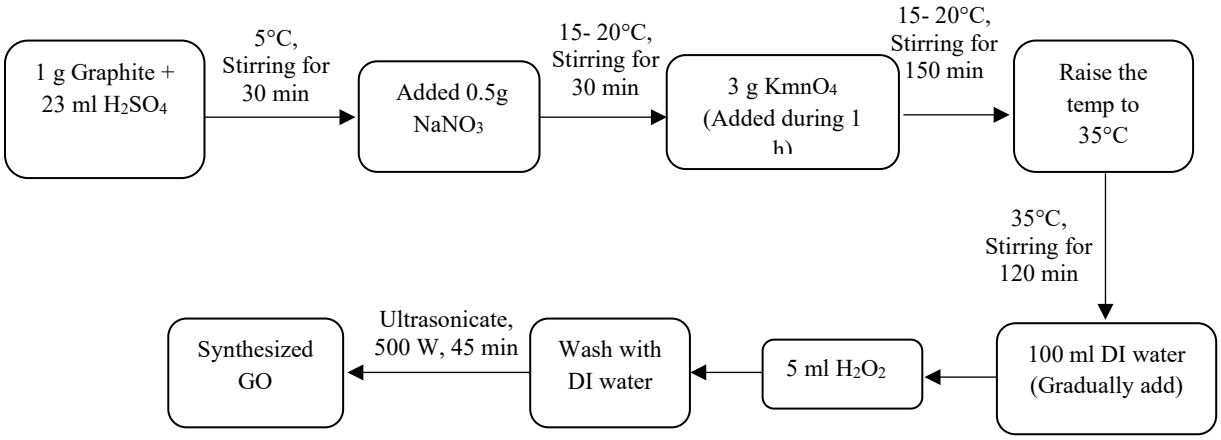

Fig. 1. Synthetic route of GO

2.4 Removal Procedure

A 10 mL solution containing 100 mg L^{-1} Pb^{2+} solution at pH 5.0 was prepared. To this solution, 20 mg of the NiCo-LDHs-rGO composite was added and the mixture was stirred at 500 rpm for 60 minutes. The concentration of Pb^{2+} remaining in the solution was quantified using atomic absorption spectroscopy. removal percentage (RP) and the adsorption capacity (q_e) were calculated using Eqs. (1) and (2), respectively.

$$RP = \frac{(C_0 - C_e)}{C_0} \times 100 \quad (1)$$

$$q_e = \frac{(C_0 - C_e) \times V}{m} \quad (2)$$

where C_e and C_0 are equilibrium and initial concentration of Pb^{2+} in mg L^{-1}, respectively, V: Sample volume in Liters, m: Adsorbent dosage in grams).

3 Results and Discussion

3.1 Characterisation of adsorbent

The formation of NiCo-LDHs-rGO can be justified by a mechanism proposed in literature [29]. According to this mechanism, thiourea is oxidised by GO resulting in formation of NH_4OH (in aqueous form) and rGO. Then, the OH^- ion reacts with Ni^{2+} and Co^{2+} leading to creation of a network of $Ni(OH)_2$ and $Co(OH)_2$ complex species on the surface of reduced GO [29, 30a]. It should be noted that organosulfur reagents such as thiourea, thiols and sulfones have proven to be useful tools for the functionalisation of organic materials [30]. We have investigated the structural features of metal-complex systems for a couple of years [31].

The synthesised NiCo-LDHs-rGO material underwent comprehensive characterisation using the FESEM, EDX, Mapping Elemental Analysis, FT-IR spectrophotometry, BET and XRD techniques. According to the FESEM images of NiCo-LDHs-rGO (presented in Fig. 2), spherical NiCo-LDHs microparticles have uniformly grown on the rGO nanosheets. The EDX analysis in Fig. 3 confirms that Co, Ni, C and O are the major elements within the structure of this composite.

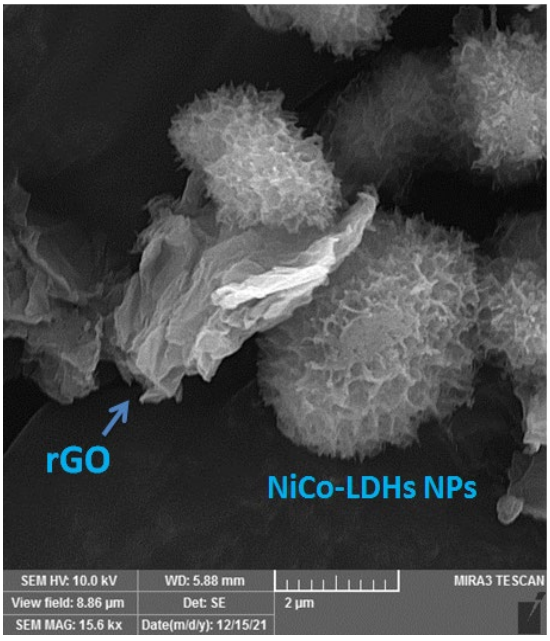

(a)

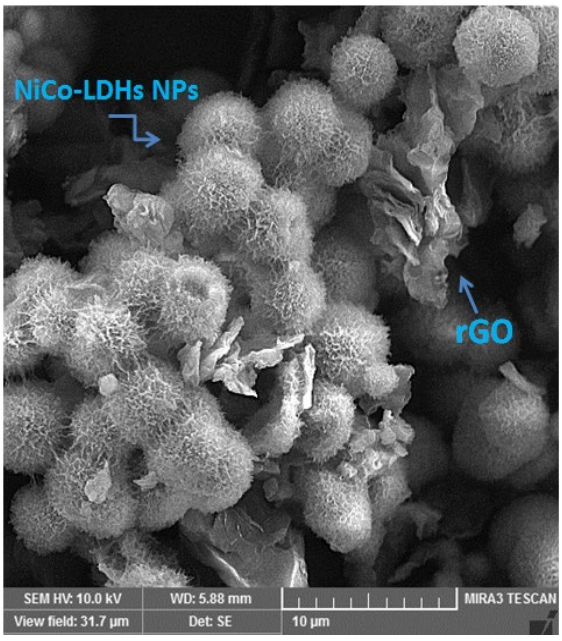

(b)

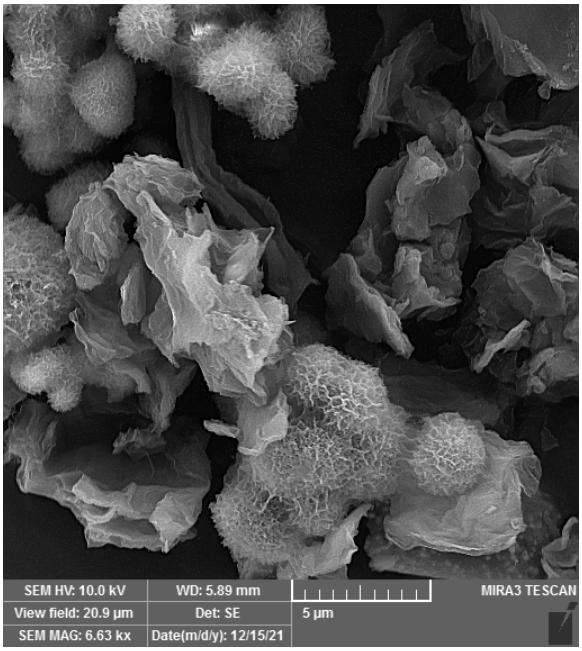

(c)

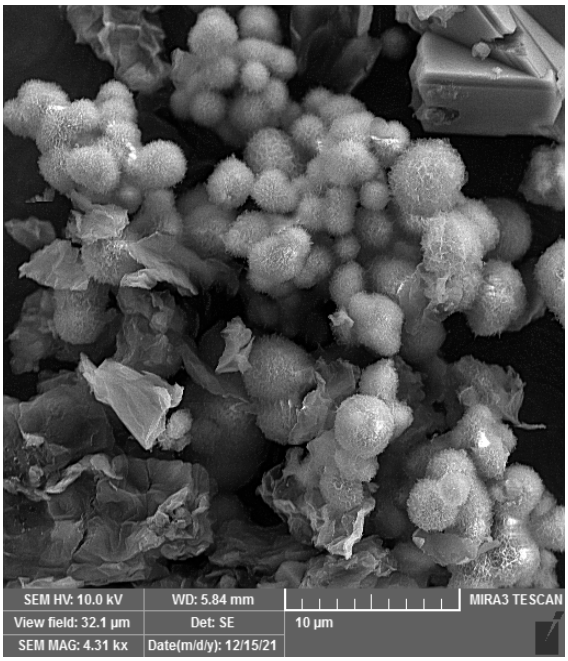

(d)

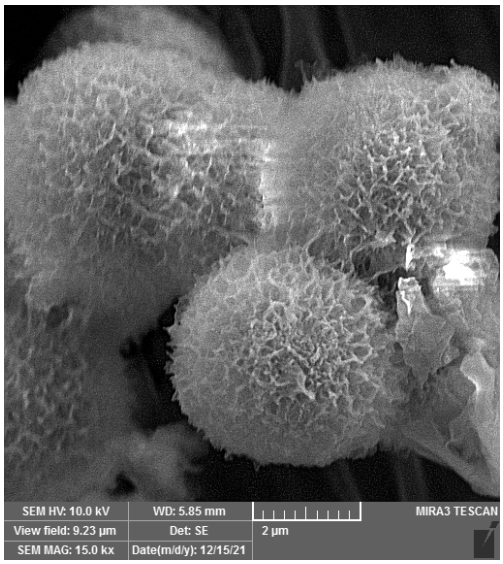

(e)

Fig. 2. FESEM images of the synthesized NiCo-LDHs-rGO.

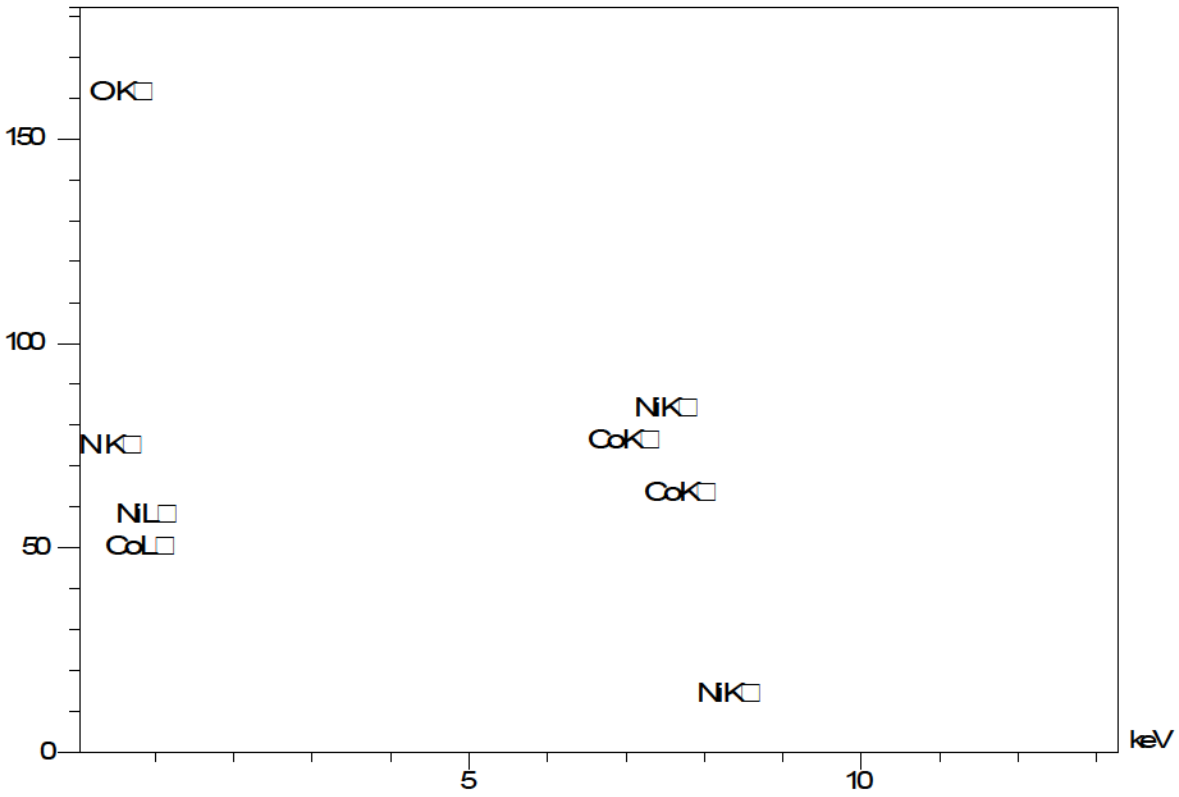

Fig. 3. EDX analysis of NiCo-LDHs-rGO

The Mapping Elemental Analysis of NiCo-LDHs-rGO, as presented in Fig 4 (4a-4d) provides a visual representation of the distribution of elements including C (4a), O (4b), Ni (4c) and Co (4d). The results show that the microspheres of NiCo-LDHs predominantly contain Ni, Co and O atoms while a higher concentration of C atoms is observed on the rGO nanosheet. Moreover, the relatively lower distribution of O atom on the rGO nanosheet serves as strong evidence for the effective conversion of GO to rGO.

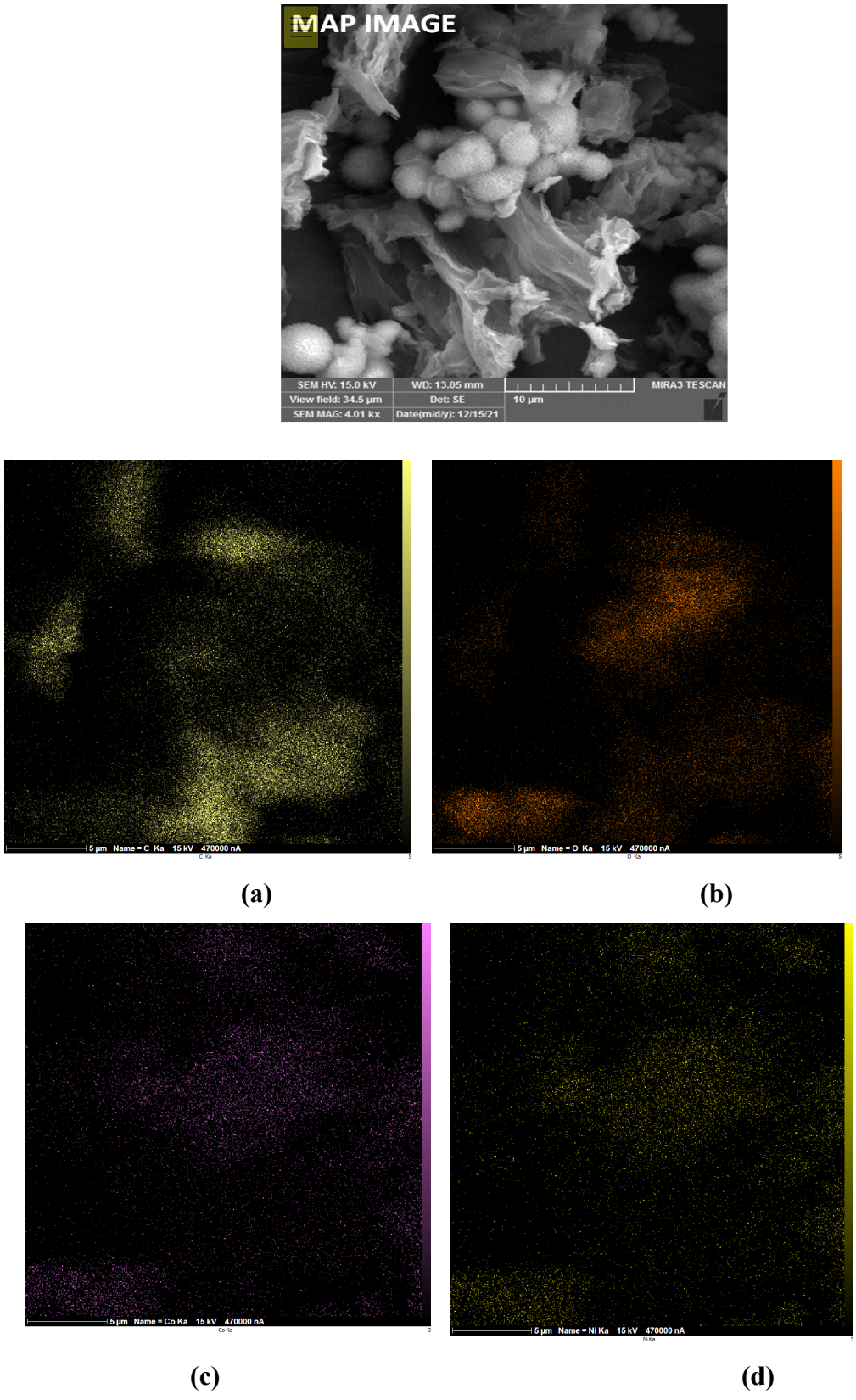

Fig. 4. MAP elemental analysis of NiCo-LDHs-rGO; distribution of elements: (a) C, (b) O, (c) Co and (d) Ni

In the FT-IR spectrum of GO (Fig. 5), several distinct bands are observed with peaks at 1050 cm^{-1}, 1220 cm^{-1}, 1730 cm^{-1} and 3400 cm^{-1} that correspond to the stretching vibrations of C-O, epoxy, carbonyl (C=O) and O-H groups, respectively [32]. However, for NiCo-LDHs-rGO, the peaks at 1388 cm^{-1} and 832 cm^{-1} are related to intercalated NO_3^- ions (Fig. 5) [33, 34]. The absorbance at 1480 cm^{-1} can be attributed to the C-H stretching vibration, while the broad band at about 650 cm^{-1} could be related to Ni-O and Co-O vibrations [34]. Moreover, the absorption band at 3400 cm^{-1} is attributed to the stretching vibration of the OH group originating from NiCo-LDHs, rGO and/or adsorbed water molecules.

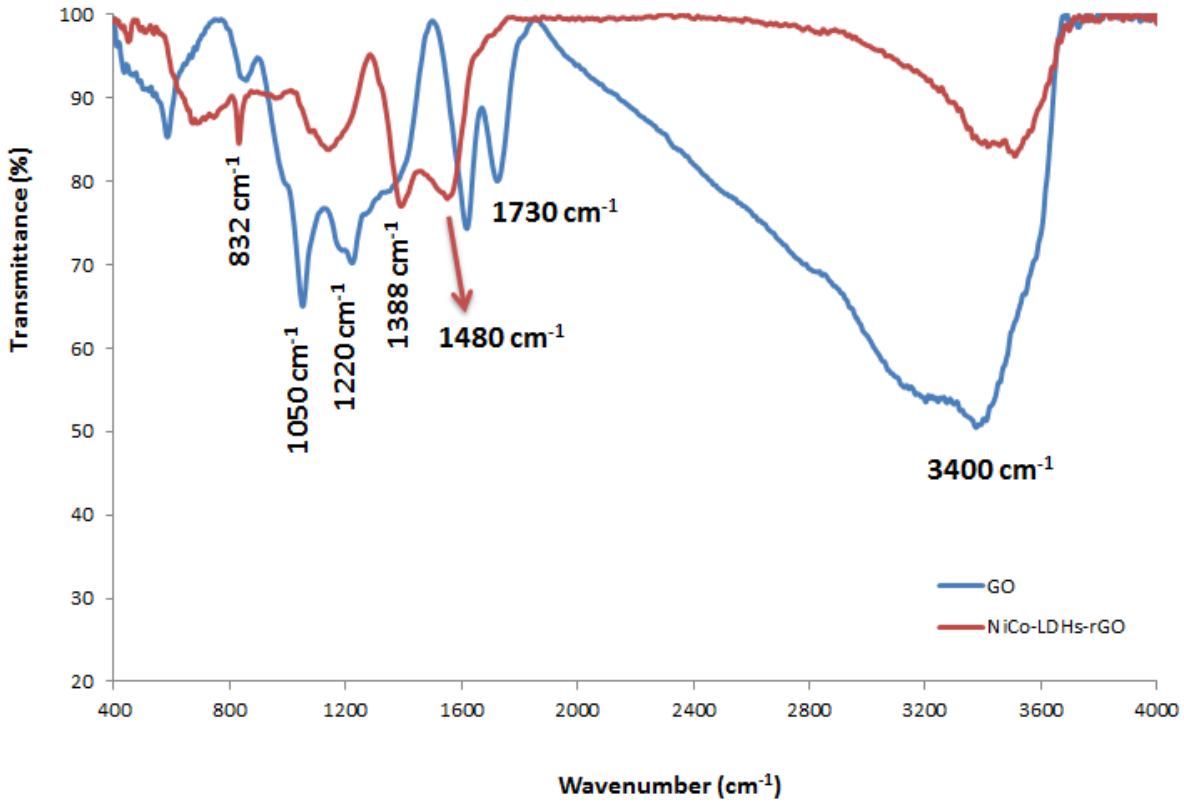

Fig. 5. FT-IR spectra of GO and synthesised NiCo-LDHs-rGO.

To calculate the surface area of NiCo-LDHs-rGO, BET analysis was conducted (results presented in Fig.S1 in *Electronic Supplementary Material*). The analysis reveals that the composite possesses slit-shaped pores (H3) due to the observed type IV isotherm with hysteresis occurring at P/P0= 0.34–0.97. Further calculations indicate an average pore diameter of 18.8 nm and a surface area of

50.2 m^2 g^{-1}, confirming the presence of mesopores within the composite (pore diameter ranging from 2 to 50 nm). Finally, XRD analysis of NiCo-LDHs-rGO (Fig.S2) shows that the diffraction peaks at 2θ value of 11.2°, 34.0°, 38.5° and 60.5° corresponding to the (003), (009), (015) and (110) crystal planes, respectively (JCPDS No. 38-0715) [35]. Moreover, the intense diffraction main peak of rGO – occurring at approximately 2θ = 24.0° confirms the effective conversion of GO to rGO [36].

3.2 Optimisation of experimental parameters

The selection of input experimental parameters, including pH, adsorbent amounts (M), and Contact Time (CT), was based on a normal statistical distribution, as illustrated in Figure 6. The average values for these parameters are provided in level II of Table 1. Furthermore, Figure 6 demonstrates the normal distribution analysis of the experimental output, RP, which also conforms to a normal statistical distribution. The Taguchi design method was used in this study to determine optimal values of three parameters with the objective of maximising RP. To initiate this process, the permissible range of these parameters, considering their respective limitations, is defined in Table 1.

Table 1. The range of the effective parameters analysed in Taguchi design model

Parameters/Levels	I	II	III
pH (A)	3.0	5.0	7.0
M (mg, B)	5.0	12.5	20.0
CT (min, C)	10.0	20.0	30.0

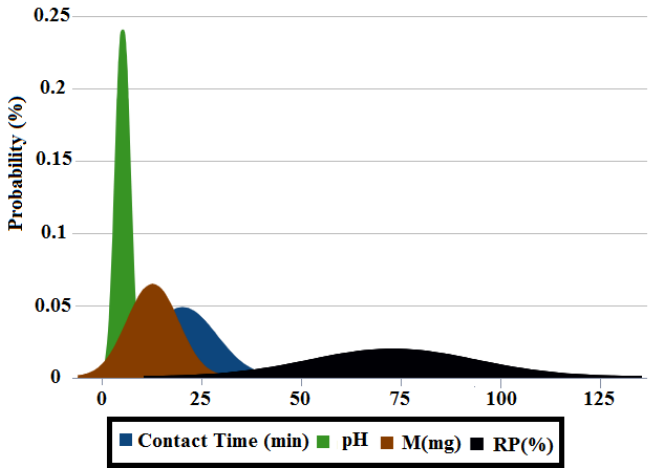

Fig. 6. Normal distribution analysis for input and output design of experiment process

The outputs of Cumulative Distribution Function (CDF) are presented in Fig. 7, illustrating the statistical analysis of RP (%) in various experiments (each curve representing a specific set of input parameters given in Table 1). The results indicate a significant enhancement in the performance of the adsorption process when the pH value is set as the second parameter (level II, pH = 5.0 as shown in Table 1). To explore the adsorption mechanism of Pb^{2+}, the pH_{PZC} of NiCo-LDHs-rGO composite was determined which was found to be 3.8. Therefore, the surface of NiCo-LDHs-rGO was negatively charged at pH>3.6 due to the deprotonation effect. Several mechanisms can explain the adsorption of Pb^{2+} onto the adsorbent: (1) Electrostatic interaction between the remaining carboxylic acid groups of rGO and Pb^{2+} (Fig. 8, mechanism 1); (2) Ion-dipolar interaction involving the hydroxyl groups of NiCo-LDHs and rGO with the Pb^{2+} ion (Fig. 8, mechanisms 2 and 3); (3) π-cation interaction between rGO and Pb^{2+} (Fig. 8, mechanism 4). Overall, it is expected that in acidic pH (level I, pH = 3.0) the RP of Pb^{2+} decreases due to the abundance of H^{+} ions which compete with Pb^{2+} ions for adsorption sites of NiCo-LDHs-rGO and hinder the dissociation of carboxylic acid group required for electrostatic interactions with Pb^{2+} ions [37-44]. Fig. 7 highlights that when all effective factors are at the first level (black line in Fig. 7), the removal percentage almost reaches to 50% at its best. However, in the optimal state (red line in Fig. 7), it can surpass 95%. Fig. S4 represents the EDX analysis of NiCo-LDHs-rGO after adsorption. The appearance of Pb^{2+} peak at 10.5 keV clearly shows that Pb^{2+} ions have been adsorbed effectively.

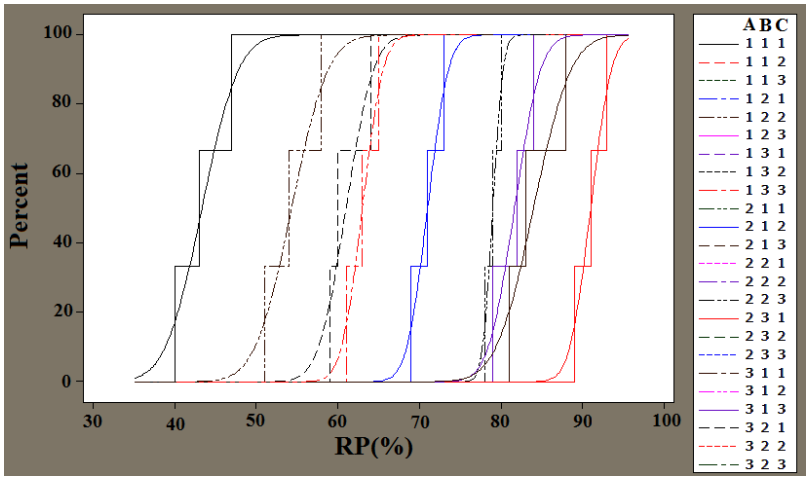

Fig. 7. Cumulative distribution function (vertical axis) of removal percentage (RP) for various parameter settings

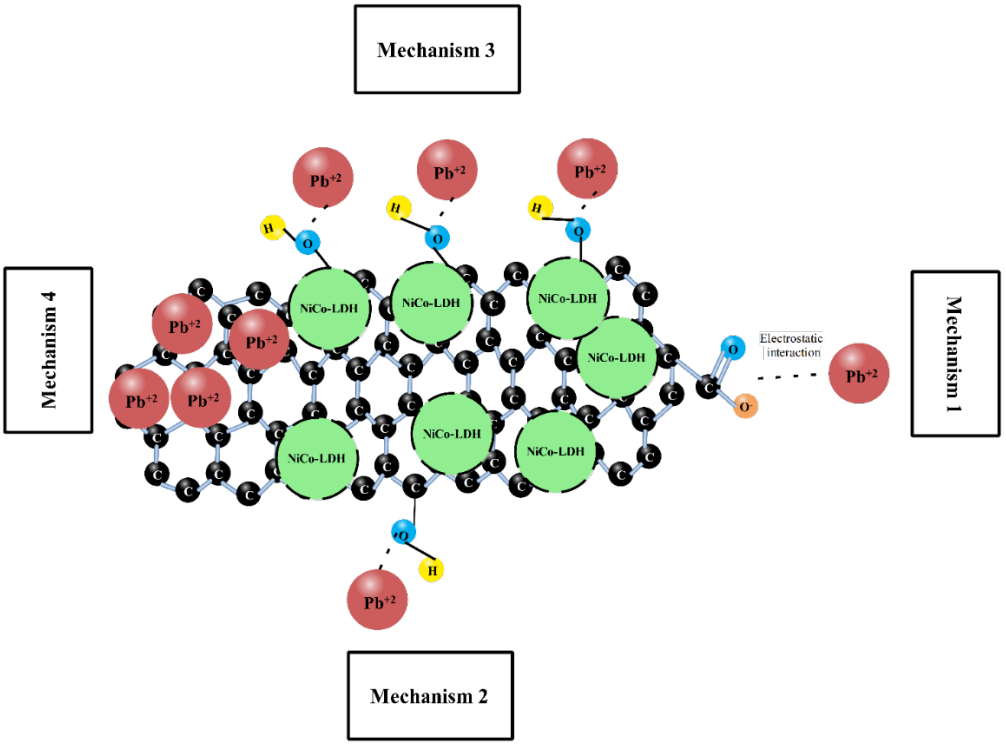

Fig. 8. The mechanism of Pb^{2+} adsorption onto the rGO-NiCo LDHs

The evaluation of signal-to-noise (S/N) ratio (Taguchi method, Fig. 9) was conducted using the Minitab 16 software. Upon analysis, it is found that for the first parameter (pH) the second level (pH = 5.0) has the highest efficiency with the highest S/N ratio value. Similarly, the optimum conditions of M and CT are related to the third values (M=20.0 mg and CT= 30.0 min). Likewise, the dual sensitive analysis of the effective parameters is illustrated in Fig. 10. Note that S/N value serves as an indicator of the signal's strength relative to noise in electrical systems [45]. In the context of the Taguchi method, this concept is used to determine the optimality of each parameter at various levels [46]. Therefore, a higher S/N value is indicative of greater system efficiency [47].

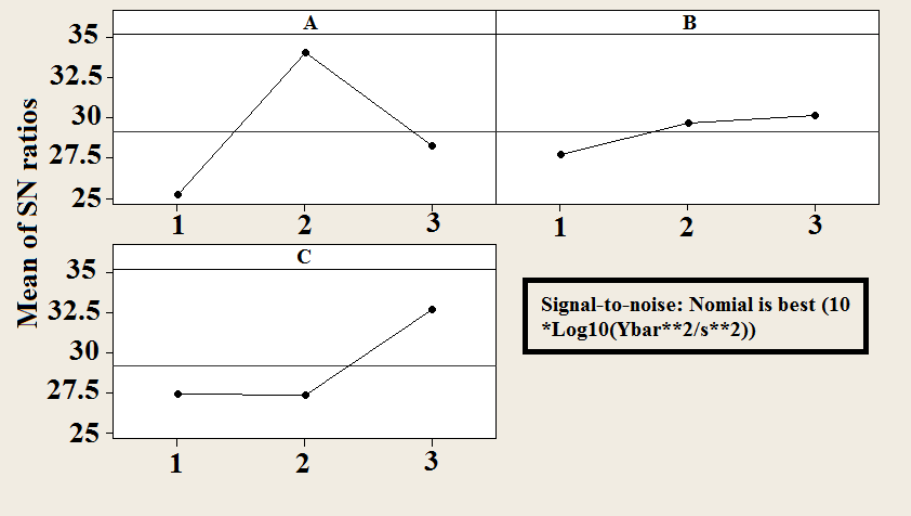

Fig. 9. Taguchi computation for main effects plot for SN ratio (A: pH, B: M, C: CT).

Fig. 10 provides a binary sensitivity analysis of the key parameters with respect to the removal efficiency. In Fig. 10a, it is evident that the slope fluctuations for pH are more pronounced compared to parameter M. This observation suggests that the obtained response (RP) is more influenced by pH than M. The analysis of Figs. 10b and 10c leads to this conclusion that pH is the most influential factor on RP. These findings highlight the significance of pH in determining RP and overall effectiveness of the decontamination process. Comparing Figs. 10-a-c reveals valuable aspects of the decontamination process using the newly synthesised composite. It is evident that A has a greater influence than B, while A has a greater influence than C, and C has a greater influence than B. Consequently, the order of importance for these parameters can be established as follows: A > C > B. Furthermore, the intensity of slope variation, Fig. 9, supports the same conclusion. The S/N (Signal-to-Noise) values obtained from A are consistently higher than those of C and B. This reaffirms the importance of A (pH) in driving the response and underscores its significant role for the optimisation of the decontamination process. By providing a more comprehensive analysis and highlighting the consistent trends, observed across multiple figures, the extended passage offers greater clarity regarding the importance of pH related to the response variable (RP), emphasising its critical role in the decontamination process.

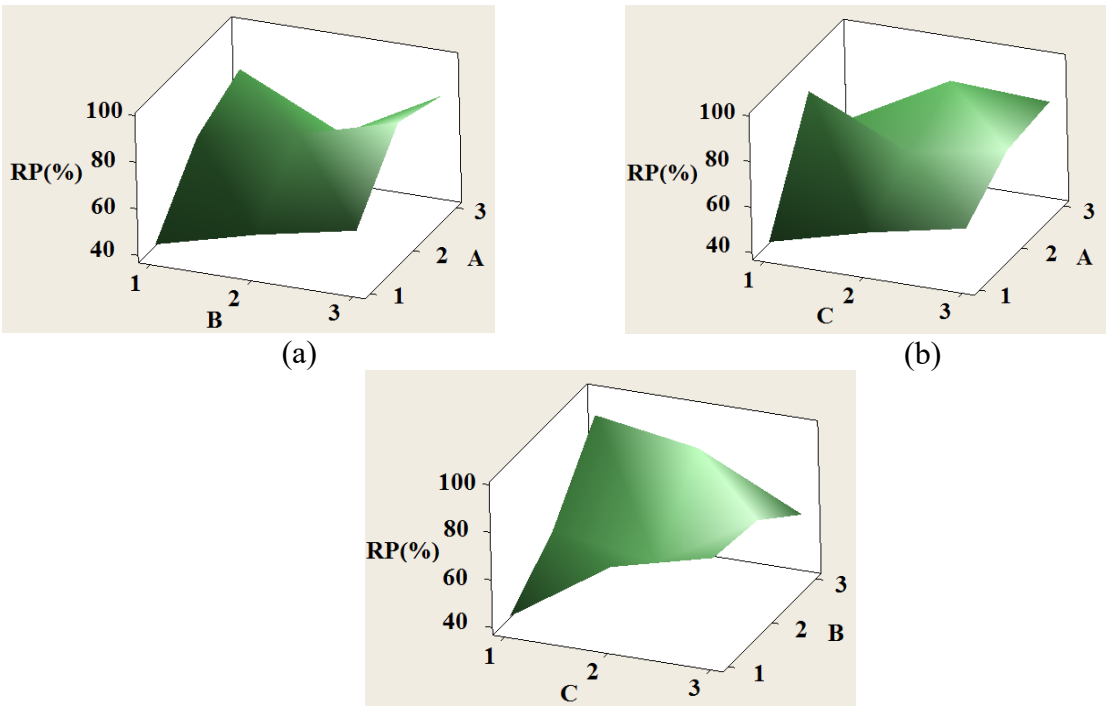

(a) (b) (c)

Fig. 10. Dual sensitive analysis of the surface plot of RP (%) between a) pH vs M, b) pH vs CT, c) M vs CT.

Based on pH, M and CT, a polynomial regression model was used to estimate RP. The correlation coefficients of quadratic models for the interpolation of M-pH (Eq. 3 and Fig. 11a), CT-pH (Eq. 4 and Fig. 11b) and M-CT (Eq. 5 and Fig. 11c) are equal to 0.62, 0.67 and 0.47, respectively. However, due to the low values of the coefficients, the proposed methods may be unable to estimate RP, and thus, it is advisable to explore machine learning computations for more accurate estimations.

$$f(x,y) = P_{00} + P_{10}x + P_{01}y + P_{20}x^2 + P_{11}xy + P_{02}y^2 \quad \text{where } x\text{=M and } y\text{=pH} \qquad (3)$$

Coefficients (with 95% confidence bounds):

P_{00} = -74 (-157.2, 9.234)

P_{10} = 52.66 (21.46, 83.86)

P_{01} = 0.1962 (-5.947, 6.339)

P_{20} = -4.246 (-7.264, -1.229)

P_{11} = -0.2695 (-0.8385, 0.2995)

P_{02} = 0.09634 (-0.1183, 0.3109)

$$f(x,y) = P_{00} + P_{10}x + P_{01}y + P_{20}x^2 + P_{11}xy + P_{02}y^2 \quad \text{where } x\text{=CT and } y\text{=pH} \qquad (4)$$

Coefficients (with 95% confidence bounds):

P_{00} = -85.21 (-170.9, 0.4487)

P_{10} = 47.66 (18.37, 76.96)

P_{01} = 2.853 (-2.09, 7.797)

P_{20} = -3.499 (-6.301, -0.6977)

P_{11} = -0.2947 (-0.6909, 0.1015)

P_{02} = -0.01909 (-0.1312, 0.09297)

$$f(x,y) = P_{00} + P_{10}x + P_{01}y + P_{20}x^2 + P_{11}xy + P_{02}y^2 \quad \text{where } x\text{=M and } y\text{=CT} \qquad (5)$$

Coefficients (with 95% confidence bounds):

P_{00} = 1.23 (-68.99, 71.45)

P_{10} = 3.595 (-3.471, 10.66)

P_{01} = 3.94 (-2.144, 10.02)

P_{20} = 0.06327 (-0.1937, 0.3202)

P_{11} = -0.1966 (-0.3329, -0.06036)

P_{02} = -0.02491 (-0.1694, 0.1196)

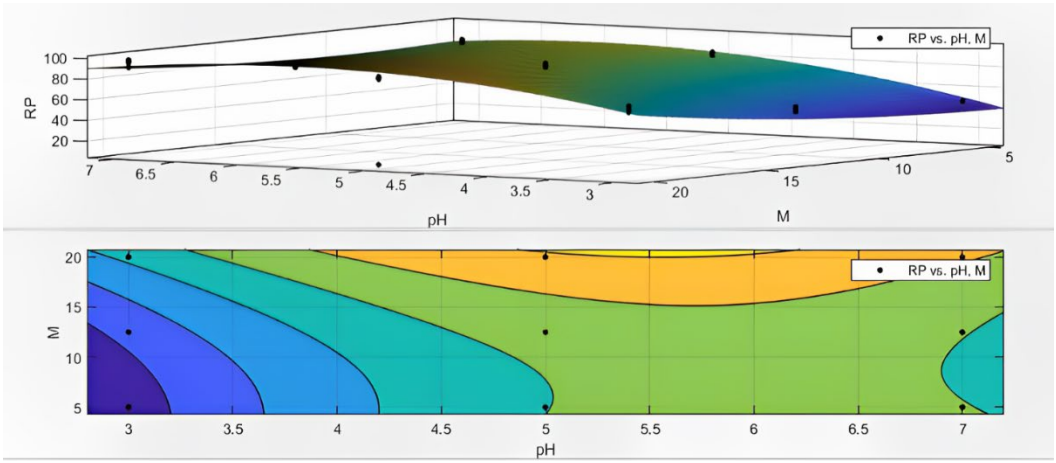

(a)

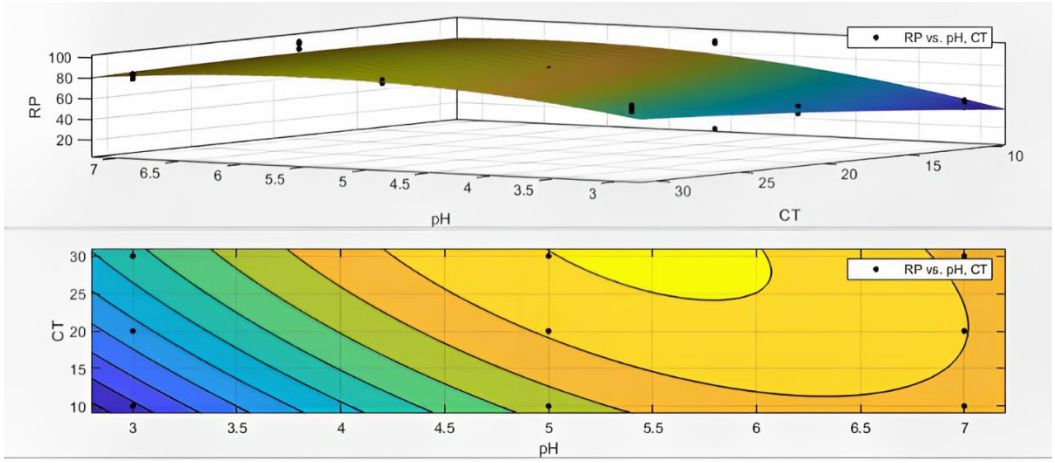

(b)

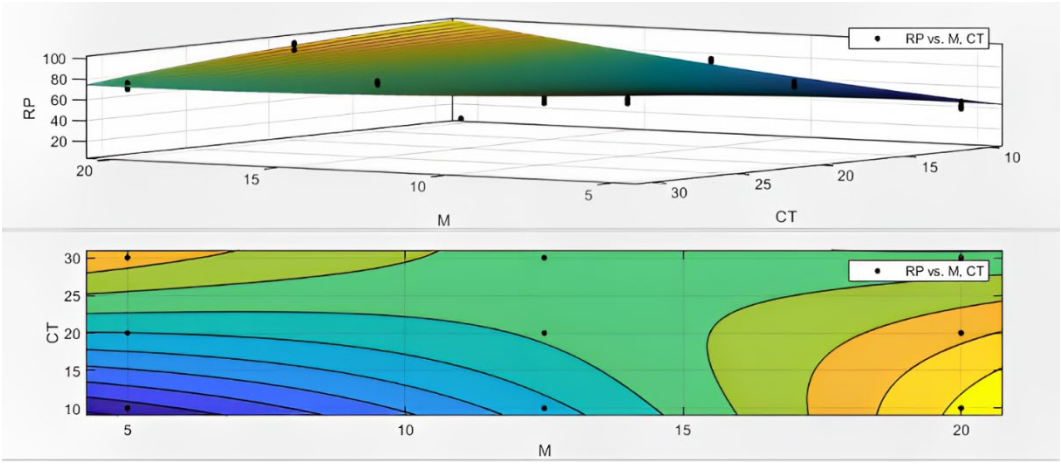

(c)

Fig. 11. Outputs of dual mathematical modeling based on RP fluctuations. a) pH-M, b) pH-CT c) M-CT.

Lazy learning, a type of machine learning computation, is primarily designed for datasets with a limited number of attribute data specifications. In the context of this research, where the characterisation of adsorption process is comparatively constrained compared to other data mining scenarios, the lazy models were applied in this study. Hence, three lazy models, i.e. lazy.IBk, lazy.KStar and lazy.LWL were investigated due to the relatively low efficiency of mathematical regression modeling. The distribution of data through data mining computations is presented in Fig. 12. To implement machine learning systems, different data structuring approaches are required. As observed in Fig. 12, the learning data is displayed as a matrix plot. Note that the data shown in this figure are derived from experimental results and thus represent the practical

outcomes of the processes. According to Table 2, it can be inferred that all the computation models have appropriate performance with a correlation coefficient more than 0.9500 for the prediction of removal percentage; the approach can fill the lack of precision in simple mathematical modeling.

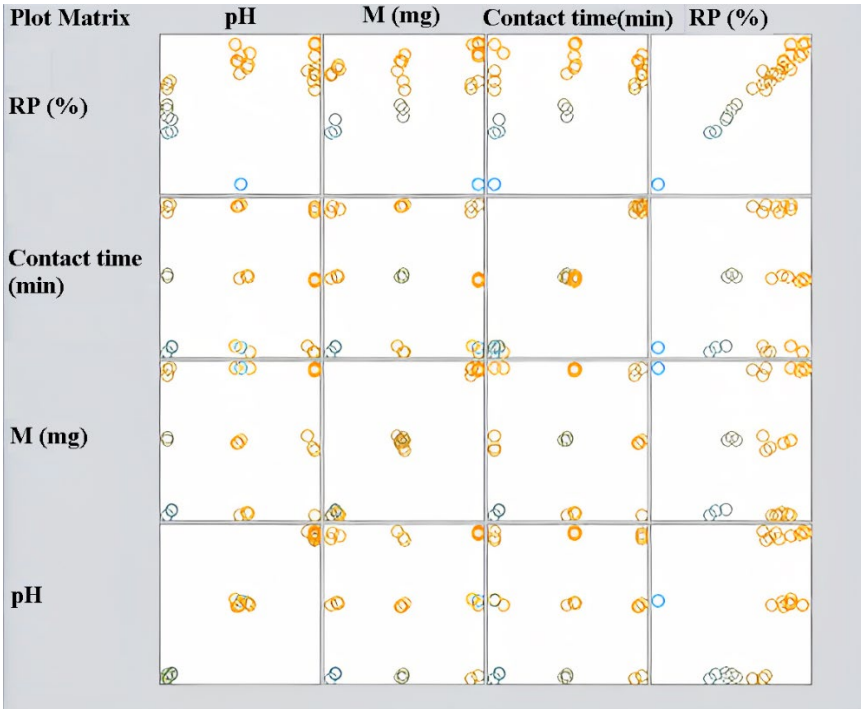

Fig. 12. Data distribution in this study.

Table 2. Results of three lazy.IBk, lazy.KStar and lazy.LWL modeling

Parameters	lazy.IBk	lazy.KStar	lazy.LWL
Correlation coefficient	0.9927	0.9922	0.9650
Mean absolute error	3.667	4.704	7.220
Root mean squared error	4.262	5.724	8.479
Relative absolute error	23.40 %	30.03 %	46.08 %
Root relative squared error	21.70 %	29.15 %	43.18 %
Description	Instances: 27 Attributes: 4 Test mode: split 66.0% train, remainder test IB1 instance-based classifier	Relation: ML Instances: 27 Attributes: 4 Test mode: split 66.0% train, remainder test KStar Beta Verion (0.1b). KStar options: -B 20 -M a	Relation: ML Instances: 27 Attributes: 4 Test mode: split 66.0% train, remainder test Locally weighted learning Using classifier: weka. classifiers.

3.3 Adsorption isotherm

3.3.1 Langmuir and Freundlich

Eq. 6 (Table S1) shows the Langmuir isotherm which is related to monolayer adsorption. The calculated values for q_{max} and K_{ads} are 200 mg g^{-1} and 13.44 L mg^{-1}, respectively (Table 3) [29]. Moreover, Eq. 7 shows the multilayer adsorption of the analyte (Table S1) based on the Freundlich isotherm. The calculated Freundlich parameters (Table 3) show that the adsorption of Pb^{2+} onto the NiCo-LDHs-rGO composite is a favourable process (n>1) [29]. Since R^2 of Langmuir (0.9930) and Freundlich (0.9860) isotherms were very close to each other, three-parameter isotherm models used to determine the accurate adsorption isotherm model [29].

Table 3. Results of interpretation of isotherm models

Isotherm	**Coefficients**			
Langmuir Isotherm	$q_{max}(mg\ g^{-1})$	$k_{ads}\ (L\ g^{-1})$	R^2	
	200	13.44	0.9930	
Freundlich Isotherm	N	k_F	R^2	
	3.99	47.55	0.9860	
Temkin Isotherm	b(J/mol)	A ($L\ mg^{-1}$)	R^2	
	93.51	4.21	0.9394	
D-R Isotherm	$q_{max}(mg\ g^{-1})$	$k_d\ (mol^2J^{-2})$	R^2	E $(kJ(mol)^{-1})$
	134	0.34	0.7061	1.30

3.3.2 Three-parameter isotherm

To precisely determine the adsorption mechanism, three-parameter isotherms including Sips [48], Kobbel-Corrigan [49], Toth [50], Khan [51] and Radke–Prausnitz [52] were used. The outcome and conditions of each isotherm are illustrated in Table 4. According to the results, it is understood that the Freundlich model – which follows the heterogeneous surface adsorption mechanism – dominated the monolayer system.

Table 4. The results of three-parameter isotherm

Three-parameter isotherm	Formulation	Description	Correlation coefficient	Selected mechanism
Sips	$q_e = \frac{k_s C_e^{b_s}}{1 + a_s C_e^{b_s}}$	If B_t converge to 1, Langmuir is the main mechanism, else, Freundlich is the appropriate mechanism	0.98	Heterogeneous surface mechanism (Freundlich)
Kobbel-Corrigan	$q_e = \frac{A C_e^{n}}{1 + B C_e^{n}}$	If n converge to 1, Langmuir is the main mechanism, else, Freundlich is the appropriate mechanism	0.98	Heterogeneous surface mechanism (Freundlich)
Toth	$q_e = \frac{k_T C_e}{(a_T + C_e)^{1/t}}$	If 1/t converge to 1, Langmuir is the main mechanism, else, Freundlich is the appropriate mechanism	0.98	Heterogeneous surface mechanism (Freundlich)
Khan	$q_e = \frac{q_s b_k C_e}{(1 + b_k C_e)^{u_k}}$	If u_t converge to 1, Langmuir is the main mechanism, else, Freundlich is the appropriate mechanism	0.98	Heterogeneous surface mechanism (Freundlich)
Adke–Prausnitz	$q_e = \frac{a_{RP} r_R C_e^{b_R}}{a_{RP} + r_R C_e^{b_R - 1}}$	If B_R-1 converge to 1, Langmuir is the main mechanism, else, Freundlich is the appropriate mechanism	0.98	Heterogeneous surface mechanism (Freundlich)

3.3.3 Dubinin–Radushkevich (DR) model

Eq. 8 (Table S1) shows the DR isotherm formula (Eqs. 9 and 10 have been used for the calculation of DR factors). According to the physical adsorption mechanism (E<8.00 kJ mol^{-1}) and the obtained E value presented in Table 3 (E=1.30 kJ mol^{-1}), it is concluded that a physio-sorption process has been occurred for Pb^{2+} adsorption [29].

3.3.4 Temkin model

Eq. 11 (Table S1) shows the Temkin model. According to value b presented in Table 3 (b = 93.51 J mol^{-1}), the Pb^{2+} adsorption is a physical process. The diagrams of Langmuir, Freundlich, DR and Temkin isotherms are presented in Fig. S5.

3.4 Adsorption kinetic

3.4.1 Pseudo first order kinetic model (PFO model)

The formula of PFO model is provided in Table S2 (Eq. 12) [29]. As described in Table 5, R^2 for Pb^{2+} are in the range of 0.6678 to 0.7459. Moreover, the calculated q_e is different than the experimental q_e; accordingly, PFO is not applicable for analysing the kinetic results.

3.4.2. Pseudo-second-order model (PSO model)

Eq. 13 (Table S2) represents the simplified form of PSO model [29]. Table 5 displays the calculated values of k_2 and R^2, so that R^2 was obtained ≥0.9800 for different Pb^{2+} concentrations. Also, q_e (cal) is so close to q_e (exp), showing that PSO is the applicable model for analysing the kinetic data.

Table 5. Results of interpretation of kinetic models

Concentration (mg L^{-1})			50	100	200	400
q_e(exp)		mg/g	51	99	177	236
PFO model	k_1	1/min	0.030	0.020	0.018	0.018
	q_e	mg/g	10	35	88	124
	R^2	-	**0.6678**	**0.7459**	**0.7020**	**0.7151**
PSO model	k_2	g/mg.min	0.0057	0.0016	0.0004	0.0003
	q_e	mg/g	52	99	182	244
	R^2	-	**0.9983**	**0.9966**	**0.9844**	**0.9802**
	H	mg/g.min	15.41	15.67	14.20	16.80
ID model	k_{id}	$mg/gmin^{0.5}$	1.90	5.10	13.13	18.46
	C_{id}	mg/g	34.49	49.20	47.10	53.65
	R^2	-	**0.7122**	**0.7734**	**0.7305**	**0.7476**

3.4.2 Intraparticle diffusion (ID) model

Eq. 14 (Table S2) displays the formula of ID model, while Fig. 13 presents the obtained ID plots for different concentrations of Pb^{2+}. As observed, the plots have two zones: 1- Faster zone contributing to the diffusion of analytes from the bulk solution to the adsorbent surface; 2- Slower zone which is related to the intraparticle diffusion [29]. The obtained R^2 values of the two zones and as well as calculated k_{int} are shown in Table 5.

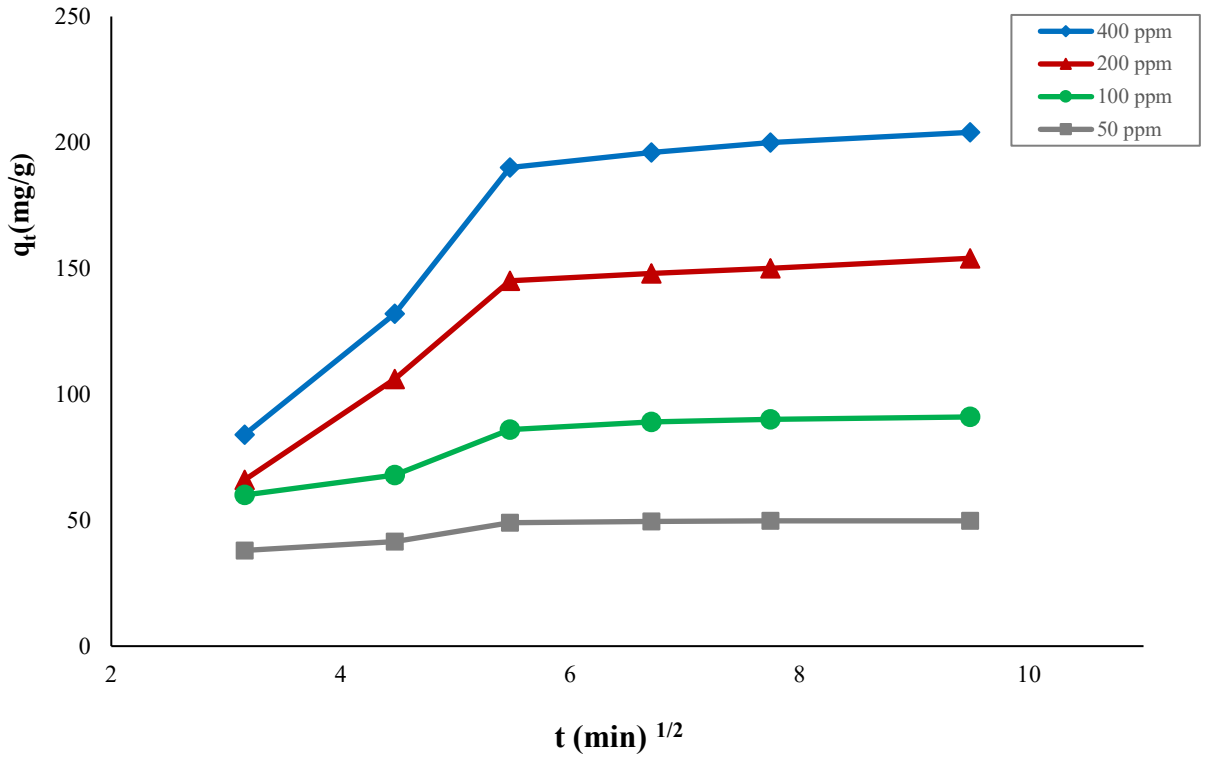

Fig. 13. ID plots for different Pb^{2+}concentrations

3.5 Simulink simulation for the kinetics of adsorption process

The research conducted in the lab scale used a Complete Mixed Reactor (CMR) which can be effectively modelled in a Simulink platform using MATLAB. In the kinetic section, PSO was selected as the most suitable model. The schematic plan of Simulink modeling process is presented in Fig. S6. Based on our kinetic study, simulation experiments were conducted for various initial concentration of Pb^{2+} (50, 100, 200 and 400 mg L^{-1}) under optimum conditions. The trends of Pb^{2+} elimination in reacting with NiCo-LDHs-rGO are illustrated in Fig. 14. All the mentioned trends have been computed by using the numerical analysis of kinetic differential equations in a Simulink platform. According to Fig. 14, it is found that the concentration of Pb^{2+} decreases over a 30-minute run (adsorption process). Fig. 15 presents the relationship between q_t and t, based on the numerical and experimental values. The main purpose of this scheme is to assess the simulated kinetic model by comparing it to the experimental kinetic outputs.

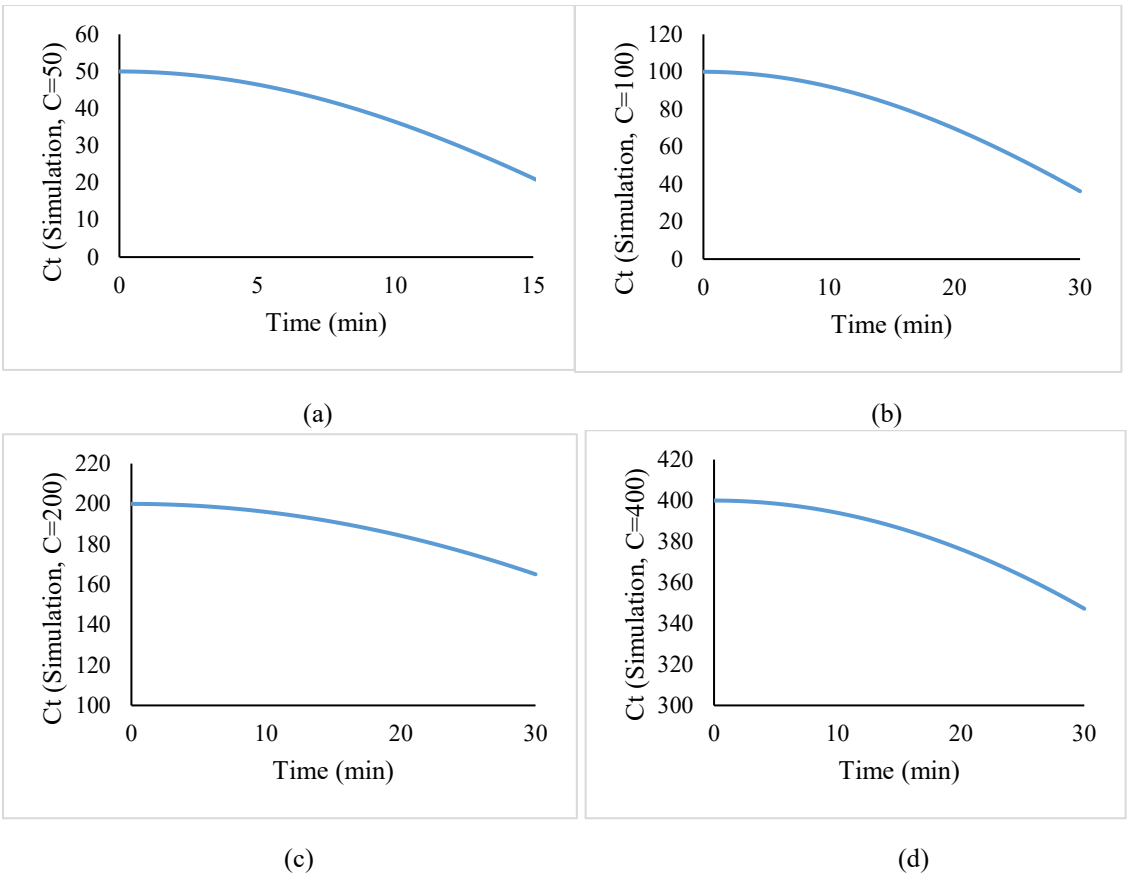

Fig. 14. Outputs of Simulink kinetic simulation in different Pb^{2+} concentrations such as (a) 50 mg L^{-1} (b) 100 mg L^{-1} (c) 200 mg L^{-1} and (d) 400 mg L^{-1}.

Analysing Fig. 15 reveals that the simulated model demonstrates a commendable level of precision in predicting q_t over time. It is worth noting that at those concentrations below 100 mg/L, the simulation and laboratory curves converge, indicating a close agreement between the simulated and experimental data. However, at higher concentrations, the convergence diminishes and then the curves begins to diverge. This divergence at higher concentrations can be attributed to the desorption process which occurs at the adsorption process progresses and the surface becomes saturated. The intricate dynamics at play in the desorption process contribute to the lower convergence observed at elevated concentrations.

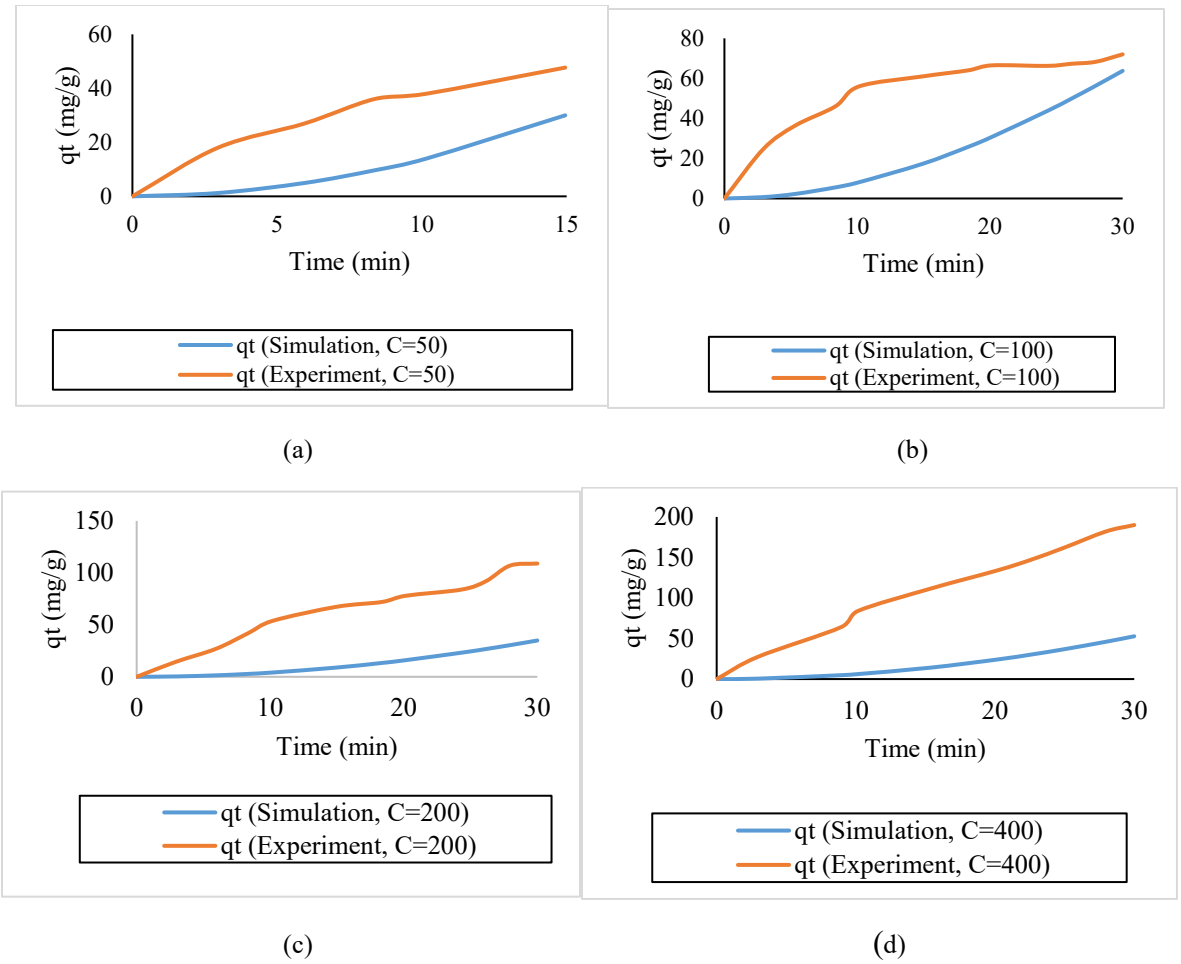

Fig. 15. Experimental/simulation kinetic evaluations of adsorption capacity outputs based on the Simulink simulation for (a) 50 mg L^{-1} (b) 100 mg L^{-1} (c) 200 mg L^{-1} and (d) 400 mg L^{-1}.

3.6 Selectivity

The adsorption selectivity for Pb^{2+} was assessed in both binary and mixed solution containing co-existing ions such as Zn^{2+}, Cu^{2+} and Cd^{2+}. As shown in Fig. S7a (for binary analysis) the uptake of Pb^{2+} using NiCo-LDHs-rGO was higher than those of the other metals, so that the selectivity sequence was determined as $Pb^{2+}>Cu^{2+}>Zn^{2+}>Cd^{2+}$. This variation in selectivity can be attributed to a range of factors including ionic radius, hydration properties and electronegativity. The selectivity of NiCo-LDHs-rGO for Pb^{2+} in a mixed solution is presented in Fig. S7b. The results indicates that the adsorption capacity of NiCo-LDHs-rGO for Pb^{2+} remained higher compared to the other ions even in the presence of a mixed solution. Moreover, the proposed NiCo-LDHs-rGO composite was applied for the removal of Pb^{2+} from the synthetic and natural wastewater samples (sourced from an industrial factory in Mashhad, Iran; Table S3). The outcomes revealed that the

NiCo-LDHs-rGO composite removed over 90.0% of Pb^{2+} contamination, indicating its high selectivity for the Pb^{2+} ion.

3.7 Reusability of adsorbent

The reusability of NiCo-LDHs-rGO was also assessed through seven consecutive adsorption/desorption cycles using HCl (0.01 mol L^{-1}) as the desorbent solution. The results in Fig. S8 confirm that the RP of Pb^{2+} experiences a gradual decrease over the cycles. After the fourth cycle, there is a 12.0% reduction in RP, however, it stabilises at approximately 87.0% for 100 mg L^{-1} of Pb^{2+} solution. By the seventh cycle, the RP drops to 70.0%, indicating that this composite can be reliably used at least for seven times with only a 20.0% reduction in RP.

3.8 Comparison with other adsorbents

Table S4 (Ref. 53-59) presents a comprehensive comparison between our synthesised NiCo-LDHs-rGO composite and other adsorbents used for the decontamination of water samples. The advantages of NiCo-LDHs-rGO – such as high adsorption capacity (200 mg g^{-1}), swift adsorption kinetics (30 minutes) and environmentally friendly and convenient synthetic approach (one-step synthesis) highlight its efficacy and efficiency as an outstanding adsorbent for the removal of Pb^{2+}.

4 Conclusions

In this study, a NiCo-LDHs-rGO composite was synthesised using a hydrothermal method and fully characterised by FT-IR, FESEM, EDX, Mapping Elemental Analysis, XRD and BET analysis. Subsequently, NiCo-LDHs-rGO was successfully employed for the efficient removal of Pb^{2+} from water samples. The advantages of this method include the simplicity of one-step synthesis for the adsorbent, rapid removal kinetics and remarkable high adsorption capacity. Our experimental findings indicated that this composite has the maximum efficiency at pH 5.0 (99.7% for 100 mg L^{-1} of Pb^{2+}). More importantly, the presences of co-existing ions did not significantly affect the removal process under these optimised conditions. our experimental data on adsorption isotherms were well-fitted to the Freundlich isotherm model, with a maximum adsorption capacity (qmax) of 200.0 mg g^{-1}. For the interpretation of kinetic results, the PSO kinetic model proved to be the most suitable equation. Moreover, the NiCo-LDHs-rGO composite demonstrated remarkable resilience, with a minimal change in performance after four regeneration cycles,

maintaining an impressive 87.0% removal percentage. This robust performance highlights the NiCo-LDHs-rGO composite as a promising, cost-effective material for the removal of Pb^{2+} from water samples. Therefore, it stands as an economical and highly effective solution for wastewater decontamination.

Conflict of interest

The authors declare no competing financial interest.

5 References

[1] G. Flora, D. Gupta, A. Tiwari, Toxicity of lead: A review with recent updates. Interdiscip. Toxicol. 5(2) (2012) 47-58.

[2] G.J. May, A. Davidson, B. Monahov, Lead batteries for utility energy storage: A review. J. Energy Storage 15 (2018) 145-157.

[3] A. Goyal, S. McKechnie, D. Pashov, W. Tumas, M. van Schilfgaarde, V. Stevanović, Origin of Pronounced Nonlinear Band Gap Behavior in Lead–Tin Hybrid Perovskite Alloys. Chem. Mater. 30 (2018) 3920-3928.

[4] Centers for Disease Control and Prevention. Lead: CDC's National Surveillance Data (1997–2015) (Centers for Disease Control and Prevention, 2016).

[5] M. Tuzen, A. Sarı, T.A. Saleh, Synthesis, characterization and evaluation of carbon nanofiber modified-polymer for ultra-removal of thorium ions from aquatic media. Chem. Eng. Res. Des. 163 (2020) 76-84.

[6] A. Sarı, T.A. Saleh, M. Tuzen, Development and characterization of polymer-modified vermiculite composite as novel highly-efficient adsorbent for water treatment. Surf. Interfaces 27 (2021) 101504.

[7] T.A. Saleh, M. Tuzen, A. Sarı, Effective antimony removal from wastewaters using polymer modified sepiolite: Isotherm kinetic and thermodynamic analysis. Chem. Eng. Res. Des. 184 (2022) 215-223.

[8] T.A. Saleh, M. Tuzen, A. Sarı, N. Altunay, Factorial design, physical studies and rapid arsenic adsorption using newly prepared polymer modified perlite adsorbent. Chem. Eng. Res. Des. 183 (2022) 181-191.

[9] I. Khan Rind, A. Sarı, M. Tuzen, M. Farooque Lanjwani, I. Karaman, T.A. Saleh, Influential antimony removal from Aquatic Solution using Graphene Nanoplatelet/Staphylococcus aureus as Novel Composite Adsorbent. Surf. Interfaces 38 (2023) 102765.

[10] I. Khan Rind, M. Tuzen, A. Sarı, M. Farooque Lanjwani, N. Memon, T.A. Saleh, Synthesis of TiO2 nanoparticles loaded on magnetite nanoparticles modified kaolinite clay (KC) and their efficiency for As(III) adsorption. Chem. Eng. Res. Des. 191 (2023) 523-536.

[11] A. Shahat, R. Awual, A. Khaleque, Z. Alam, M. Naushad, A.M. Sarwaruddin Chowdhury, Large-pore diameter nano-adsorbent and its application for rapid lead(II) detection and removal from aqueous media. Chem. Eng. J. 273 (2015) 286-295.

[12] R. Awual, An efficient composite material for selective lead(II) monitoring and removal from wastewater. J. Environ. Chem. Eng. 7 (2019) 103087.

[13] R. Awual, A. Islam, M. Hasan, M.M. Rahman, A.M. Asiri, A. Khaleque, C. Sheikh, Introducing an alternate conjugated material for enhanced lead(II) capturing from wastewater. J. Clean. Prod. 224 (2019) 920-929.

[14] R. Awual, M. Hasan, A. Islam, M.M. Rahman, A.M. Asiri, A. Khaleque, C. Sheikh, Offering an innovative composited material for effective lead(II) monitoring and removal from polluted water. J. Clean. Prod. 231 (2019) 214-223.

[15] A. Makarem, M. Gheibi, R. Mirsafaei, M. Eftekhari, Hydrothermally synthesized tannic acid-copper(I) complex-based nanoparticles for efficient decontamination of lead ions from aqueous solutions. J. Mol. Liq. 388 (2023) 122743.

[16] N. Rezazadeh, S. Danesh, M. Eftekhari, TX-100 adsorption from aqueous solution using modified graphene oxide; optimization by response surface methodology and one factor at a time techniques. J. Dispers. Sci. Technol. 44 (2023) 889-900.

[17] Q. Zhang, Q. Hou, G. Huang, Q. Fan, Removal of heavy metals in aquatic environment by graphene oxide composites: a review. Environ. Sci. Pollut. Res. 27 (2020) 190-209.

[18] J.Y. Lim, N.M. Mubarak, E.C. Abdullah, S. Nizamuddin, M. Khalid, Inamuddin, Recent trends in the synthesis of graphene and graphene oxide based nanomaterials for removal of heavy metals- A review. J. Ind. Eng. Chem. 66 (2018) 29-44.

[19] M. Majdoub, A. Amedlous, Z. Anfar, A. Jada, N. El Alem, Engineering of amine-based binding chemistry on functionalized graphene oxide/alginate hybrids for simultaneous and efficient removal of trace heavy metals: Towards drinking water. J. Colloid Interface Sci. 589 (2021) 511-524.

[20] A. Shahzad, W. Miran, K. Rasool, M. Nawaz, J. Jang, S.R. Lim, D.S. Lee, Heavy metals removal by EDTA-functionalized chitosan graphene oxide nanocomposites. RSC Adv. 7 (2017) 9764-9771.

[21] M. Eftekhari, M. Gheibi, M. Akrami, F. Iranzad, Solid-phase extraction of ultra-trace levels of lead using tannic acid-coated graphene oxide as an efficient adsorbent followed by electrothermal atomic absorption spectrometry; response surface methodology – central composite design. New J. Chem. 42 (2018) 1159-1168.

[22] D. Ghadirimoghaddam, M. Gheibi, M. Eftekhari, Graphene oxide-cyanuric acid nanocomposite as a novel adsorbent for highly efficient solid phase extraction of Pb^{2+} followed by electrothermal atomic absorption spectrometry; statistical, soft computing and mechanistic efforts. Inter. J. Environ. Anal. Chem. 103 (2023) 469-490.

[23] J. Cao, Q. Mei, R. Wu, W. Wang, Flower-like nickel–cobalt layered hydroxide nanostructures for super long-life asymmetrical supercapacitors. Electrochim. Acta 321 (2019) 134711.

[24] J. Jiang, A. Zhang, L. Li, L. Ai, Nickel–cobalt layered double hydroxide nanosheets as high-performance electrocatalyst for oxygen evolution reaction. J. Power Sources 278 (2015) 445-451.

[25] M.V. Bukhtiyarova, A review on effect of synthesis conditions on the formation of layered double hydroxides. J. Solid State Chem. 269 (2019) 494-506.

[26] M.F. Warsi, I. Shakir, M. Shahid, M. Sarfraz, M. Nadeem, Z.A. Gilani, Conformal Coating of Cobalt-Nickel Layered Double Hydroxides Nanoflakes on Carbon Fibers for High-performance Electrochemical Energy Storage Supercapacitor Devices. Electrochim. Acta 135 (2014) 513-518.

[27] Y. Chen, T. Liu, L. Zhang, J. Yu, $NiCo_2S_4$ Nanotubes Anchored 3D Nitrogen-Doped Graphene Framework as Electrode Material with Enhanced Performance for Asymmetric Supercapacitors. ACS Sustainable Chem. Eng. 7 (2019) 11157-11165.

[28] Z. Lv, Q. Zhong, Y. Bu, In Site Growth of Crosslinked Nickel–Cobalt Hydroxides@Carbon Nanotubes Composite for a High-Performance Hybrid Supercapacitor. Adv. Mater. Interfaces 5 (2018) 1800438.

[29] R. Li, Z. Hu, X. Shao, P. Cheng, S. Li, W. Yu, W. Lin, D. Yuan, Large Scale Synthesis of NiCo Layered Double Hydroxides for Superior Asymmetric Electrochemical Capacitor. Sci. Rep. 6 (2016) 18737.

[30] a) K. Satheesh, R. Jayavel, Synthesis and electrochemical properties of reduced graphene oxide via chemical reduction using thiourea as a reducing agent. Mater. Lett. 113 (2013) 5-8; b) B. Akhlaghinia, A. Makarem, Dithioacetalization of carbonyl compounds under catalyst-

free condition. J. Sulfur Chem. 32 (2011) 575-581; c) K.D. Klika, C. Da Pieve, K. Kopka, G. Smith, A. Makarem, Synthesis and application of a thiol-reactive HBED-type chelator for development of easy-to-produce Ga-radiopharmaceutical kits and imaging probes. Org. Biomol. Chem., 19 (2021) 1722-1726.

[31] a) K.D. Klika, R. Alsalim, M. Eftekhari, A. Makarem, Synthesis of a polyaminocarboxylate-based aluminum complex and its structural studies using $^{1}H\{^{13}C\}$-HMBC NMR and a Karplus-Type Function. Dalt. Trans. 51 (2022) 12436-12441; b) A. Makarem, M. Konrad, C. Liolios, K. Kopka, A convenient synthesis for HBED-CC-tris(*tert*-butyl ester). Synlett 29 (2018) 1239-1243; c) A. Makarem, M.K. Sarvestani, K.D. Klika, K. Kopka, A multifunctional HBED-type chelator with dual conjugation capabilities for radiopharmaceutical development. Synlett 30 (2019) 1795-1798; d) A. Makarem, K.D. Klika, G. Litau, Y. Remde, K. Kopka, HBED-NN: A bifunctional chelator for constructing radiopharmaceuticals. J. Org. Chem. 84 (2019) 7501-7508.

[32] M. Eftekhari, M. Akrami, M. Gheibi, H. Azizi-Toupkanloo, A.M. Fathollahi-Fard, G. Tian, Cadmium and copper heavy metal treatment from water resources by high-performance folic acid-graphene oxide nanocomposite adsorbent and evaluation of adsorptive mechanism using computational intelligence, isotherm, kinetic, and thermodynamic analyses. Environ. Sci. Pollut. Res. 27 (2020) 43999-44021.

[33] R. Li, Z. Hu, X. Shao, P. Cheng, S. Li, W. Yu, W. Lin, D. Yuan, Large Scale Synthesis of NiCo Layered Double Hydroxides for Superior Asymmetric Electrochemical Capacitor. Sci. Rep. 6 (2016) 18737.

[34] T. Dong, X. Zhang, M. Li, P. Wang, P. Yang, Hierarchical flower-like Ni–Co layered double hydroxide nanostructures: synthesis and super performance. Inorg. Chem. Front. 5 (2018) 3033-3041.

[35] Y. Ouyang, T. Xing, Y. Chen, L. Zheng, J. Peng, C. Wu, B. Chang, Z. Luo, X. Wang, Hierarchically structured spherical nickel cobalt layered double hydroxides particles grown on biomass porous carbon as an advanced electrode for high specific energy asymmetric supercapacitor. J. Energy Storage 30 (2020) 101454.

[36] L. Zhang, P. Cai, Z. Wei, T. Liu, J. Yu, A.A. Al-Ghamdi, S. Wageh, Synthesis of reduced graphene oxide supported nickel-cobalt-layered double hydroxide nanosheets for supercapacitors. J. Colloid Interface Sci. 588 (2021) 637-645.

[37] Y. Zheng, B. Cheng, J. Fan, J. Yu, W. Ho, Review on nickel-based adsorption materials for Congo red. J. Hazard. Mater. 403 (2021) 123559.

[38] X, Wang, B. Cheng, L. Zhang, J. Yu, Y. Li, Synthesis of MgNiCo LDH hollow structure derived from ZIF-67 as superb adsorbent for Congo red. J. Colloid Interface Sci. 612 (2022) 598-607.

[39] S. Salman, C. Sheikh, M. Hasan, N. Hasan, K.T. Kubra, et al., Chitosan-coated cotton fiber composite for efficient toxic dye encapsulation from aqueous media. Appl. Surf. Sci. 662 (2023) 157008.

[40] S. Salman, N. Hasan, M. Hasan, K. Tul Kubra, C. Sheikh, A. Islam Rehan, R.M. Waliullah, A. Islam Rasee, E. Awual, M.S. Hossain, A.K.D. Alsukaibi, H.M. Alshammari, R. Awual, Improving copper(II) ion detection and adsorption from wastewater by the ligand-functionalized composite adsorbent. J. Mol. Struct. 1282 (2023) 135259.

[41] M. Hasan, K. Tul Kubra, N. Hasan, E. Awual, S. Salman, C. Sheikh, A. Islam Rehan, A. Islam Rasee, R.M. Waliullah, S. Islam, S. Khandaker, A. Khandaker, M.S. Hossain, A.K.D. Alsukaibi, H.M. Alshammari, R. Awual, Sustainable ligand-modified based composite material for the selective and effective cadmium(II) capturing from wastewater. J. Mol. Liq. 371 (2023) 121125.

[42] T. Saadati, M. Eftekhari, N. Rezazadeh, M.K. Nazarabad, Graphene oxide–bismuth tungstate (GO–Bi2WO6) nanocomposite as a green adsorbent for lead removal: isotherm, kinetics and thermodynamic study. Int. J. Environ. Sci. Technol. 20 (2023) 1301–1314.

[43] M. Soylak, M. Tuzen, Diaion SP-850 resin as a new solid phase extractor for preconcentration-separation of trace metal ions in environmental samples. J. Hazard. Mater. 137 (2006) 1496-1501.

[44] M. Soylak, R. Sungur Cay, Separation/preconcentration of silver(I) and lead(II) in environmental samples on cellulose nitrate membrane filter prior to their flame atomic absorption spectrometric determinations. J. Hazard. Mater. 146 (2007) 142-147.

[45] S.K. Karna, R. Sahai, An overview on Taguchi method. Inter. J. Engin. Math. Sci. 1(1) (2012) 1-7.

[46] A. Mitra, The taguchi method. WIREs Comp. Stats. 3(5) (2011) 472-480.

[47] P. Yan, F. Li, Z. Liu, L. Li, Sensitivity analysis of die structural and process parameters in porthole die extrusion of magnesium alloy tube using Taguchi method. Int. J. Adv. Manuf. Technol. 119(11) (2022) 8039-8056.

[48] R. Sips, On the Structure of a Catalyst Surface. J. Chem. Phys. 16 (1948) 490–495.

[49] R.A. Koble, T.E. Corrigan, Adsorption isotherms for pure hydrocarbons. Ind. Eng. Chem. 44 (1952) 383–387.

[50] J. Toth, Acta Chem. Acad. Hung. 69 (1971) 311–317.

[51] A.R. Khan, R. Ataullah, A. Al-Haddad, Equilibrium Adsorption Studies of Some Aromatic Pollutants from Dilute Aqueous Solutions on Activated Carbon at Different Temperatures. J. Colloid Interface Sci. 194 (1997) 154–165.

[52] K. Vijayaraghavan, T.V.N. Padmesh, K. Palanivelu, M. Velan, Biosorption of nickel(II) ions onto Sargassum wightii: application of two-parameter and three-parameter isotherm models. J. Hazard. Mater. B133 (2006) 304–308.

[53] R. Sahraei, M. Ghaemy, Synthesis of modified gum tragacanth/graphene oxide composite hydrogel for heavy metal ions removal and preparation of silver nanocomposite for antibacterial activity. Carbohydr. Polym. 157 (2017) 823-833.

[54] M. Eftekhari, M. Gheibi, H. Azizi-Toupkanloo, Z. Hossein-Abadi, M. Khraisheh, A.M. Fathollahi-Fard, G. Tian, Statistical optimization, soft computing prediction, mechanistic and empirical evaluation for fundamental appraisal of copper, lead and malachite green adsorption. J. Ind. Inf. Integr. 23 (2021) 100219.

[55] Y. Li, R. Zhao, S. Chao, B. Sun, C. Wang, X. Li, Polydopamine coating assisted synthesis of MnO_2 loaded inorganic/organic composite electrospun fiber adsorbent for efficient removal of Pb^{2+} from water. Chem. Engin. J. 344 (2018) 277-289.

[56] P. Pal, A. Pal, Enhanced Pb^{2+} removal by anionic surfactant bilayer anchored on chitosan bead surface. J. Mol. Liq. 248 (2017) 713-724.

[57] F. Vasheghani Farahani, M.H. Amini, S.H. Ahmadi, S.A. Zakaria, Investigation of layered double hydroxide/carbon dot nanocomposite on removal efficiency of Pb^{2+} from aqueous solution. J. Mol. Liq. 338 (2021) 116774.

[58] Y. Zhang, Y. Liu, X. Wang, Z. Sun, J. Ma, T. Wu, F. Xing, J. Gao, Porous graphene oxide/carboxymethyl cellulose monoliths, with high metal ion adsorption. Carbohydr. Polym. 101 (2014) 392-400.

[59] M. Yuan, T. Xie, G. Yan, Q. Chen, L. Wang, Effective removal of Pb^{2+} from aqueous solutions by magnetically modified zeolite. Powder Technol. 332 (2018) 234-241.